



Phase transformation in wet chemically synthesized Y_2NiFeO_6 , and its magnetic and energy storage properties

Manju Devi¹ · Ashok Kumar² · Ashavani Kumar¹

Received: 21 May 2020 / Accepted: 11 July 2020 / Published online: 20 July 2020
© Springer-Verlag GmbH Germany, part of Springer Nature 2020

Abstract

In this work we report, the structural, magnetic, and energy storage properties of double perovskite oxide Y_2NiFeO_6 synthesized via wet chemical sol–gel process. The amorphous phase structure obtained at the synthesis temperature of 650 °C, turned to mixed cubic-hexagonal phase of Y_2NiFeO_6 at 850 °C, and subsequently to thermally stable mixed cubic-orthorhombic phase at and above the temperature of 950 °C. The X-ray photoelectron spectra of thermally stable phase of Y_2NiFeO_6 exhibited the presence of yttrium in Y^{3+} state, nickel in Ni^{2+}/Ni^{3+} state and iron in Fe^{3+} state. The Y_2NiFeO_6 exhibited room temperature ferromagnetic behavior with Curie temperature at or above the room temperature. The highest specific capacitance achieved via cyclic voltammetry in three-electrode system was 74.10 F/g at the scan rate of 5 mV/s. It has remarkable specific capacitance retention of ~95% after 5000 charging/discharging cycles at the current density of 6 A/g. The energy storage parameters i.e., energy density and power density were ~3.93 Wh/kg and ~810.03 Wkg⁻¹, respectively at current density of 1 A g⁻¹.

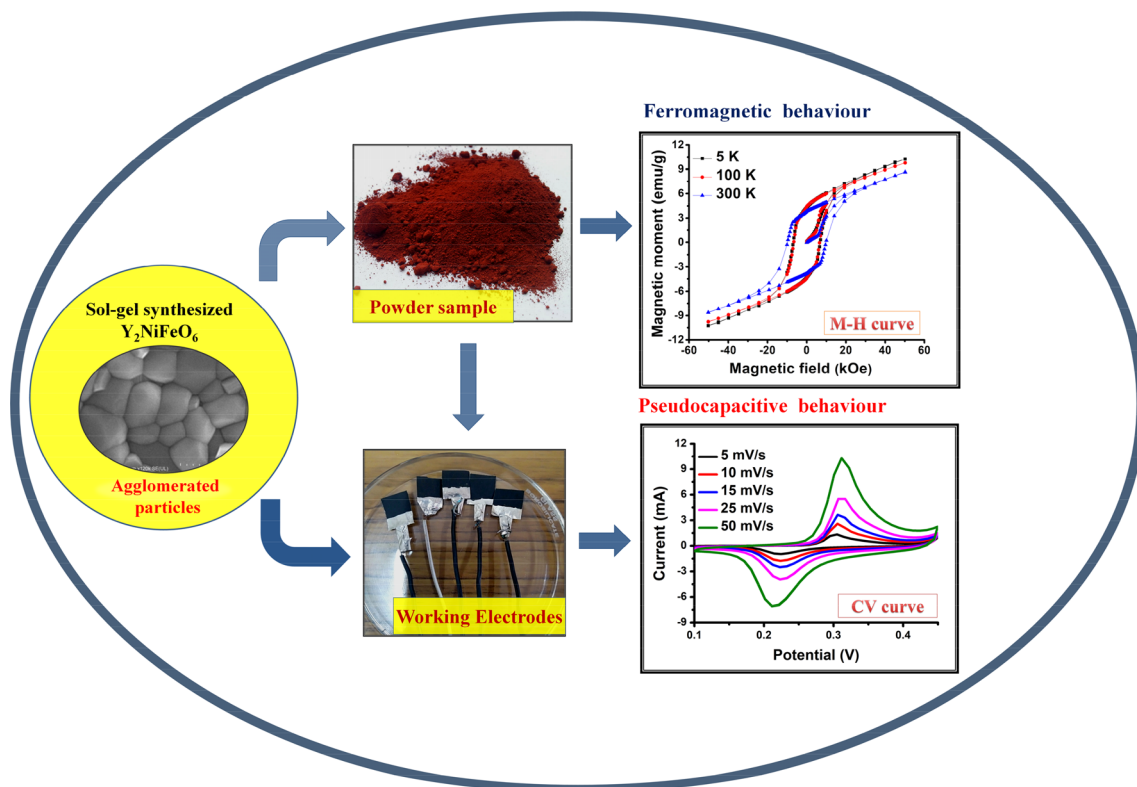
✉ Ashok Kumar
ashokku@nitttrchd.ac.in

✉ Ashavani Kumar
ashavani@yahoo.com

¹ Department of Physics, National Institute of Technology Kurukshetra, Haryana 136119, India

² Department of Applied Sciences, National Institute of Technical Teachers' Training and Research Chandigarh, Chandigarh 160019, India

Graphic abstract



Keywords Double perovskites · Wet chemical sol–gel · Magnetic behavior · Energy storage behavior

1 Introduction

The properties of double perovskites, $\text{A}_2\text{BB}'\text{O}_6$, can be tailored by substituting different metal cations at B and B' positions [1,2]. In this work yttrium, nickel and iron have been substituted in place of A, B, B'. The substitution of magnetic metals leads to magnetic behavior in the material. The magnetic behavior of double perovskite has been pursued, as these materials have multifunctional properties such as magnetoresistance, spintronic, magnetocaloric effect and multiferroicity [3–7]. Materials with Sr at A position (Sr_2CrWO_6 , $\text{Sr}_2\text{FeCoO}_6$) have been found to reveal giant magnetoresistive behavior which makes them good candidate for data storage application [6,7]. Some of the double perovskite oxides with yttrium at A position (Y_2CoMnO_6 , Y_2NiMnO_6 , Y_2FeCoO_6 , Y_2NiCoO_6), studied for magnetic behavior, have recently being investigated for energy storage applications [8–11]. The substitution of multi-oxidation state transition metals is responsible for faradic reactions in these materials. Double perovskites with lanthanum at A position have been found to possess good energy storage performance

because of high conductivity of lanthanum [12–14]. Besides, the oxygen deficient double perovskites found to have efficient energy storage behavior as a result of bulk intercalation mechanism [15–18]. The double perovskite materials have been widely synthesized by wet chemical sol–gel, solvothermal, hydrothermal, solid-state reaction, flux method, and Pechini method etc. [14,19–23]. The wet chemical sol–gel synthesis method provides several advantages such as atomic level mixing of species, high yield at low reaction temperature, higher purity and enhanced homogeneity, etc. [21,24]."

The current work focuses on the structural, magnetic, and energy storage properties of novel double perovskite Y_2NiFeO_6 . Here, Y_2NiFeO_6 , has successfully been synthesized first time by wet chemical sol–gel route. It has the Curie temperature at or above the room temperature which makes it a potential candidate for nanomagnetic application. Analysis of different experimental techniques used to investigate the energy storage behavior exhibited pseudocapacitive nature of Y_2NiFeO_6 with remarkable cyclic stability of 95% after 5000 charging–discharging cycles at the current density of 6 A/g.

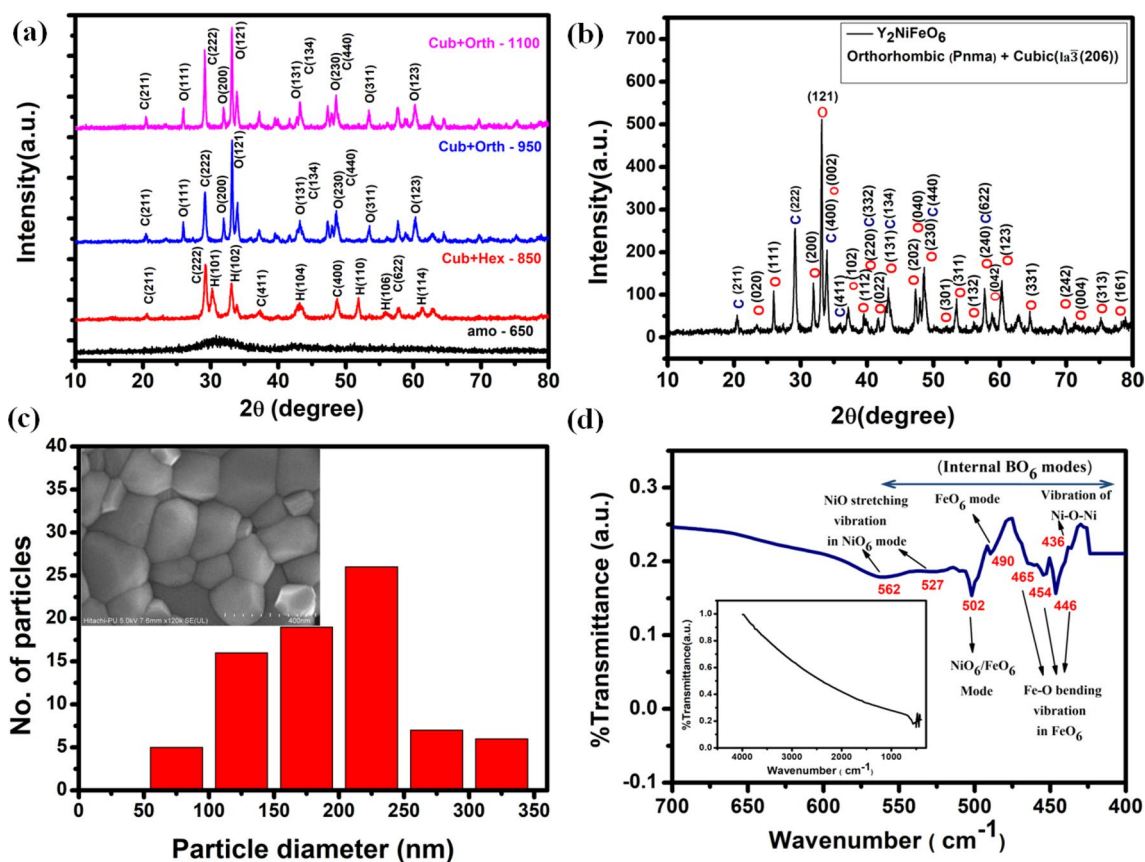


Fig. 1 **a** X-ray diffraction pattern for sample synthesized at 650 °C, 850 °C, 950 °C and 1100 °C, **b** X-ray diffraction pattern for sample synthesized at 950 °C, **c** The particle size distribution plot; (inset) FESEM for powder sample and **d** Fourier transform infrared spectrum of Y_2NiFeO_6

2 Experimental

Wet chemical sol–gel process has been employed to synthesize double perovskite oxide Y_2NiFeO_6 . Yttrium nitrate hexahydrate (99.9%), nickel nitrate hexahydrate (99%), and iron (III) nitrate nonahydrate (98%) were used as precursors, and citric acid monohydrate (99.5–102%) and ethylene glycol were used as additives. All the precursors were mixed in stoichiometric ratio in 50 ml of deionized water ($Y(NO_3)_3 \cdot 6H_2O$ —10 mmol, $Ni(NO_3)_2 \cdot 6H_2O$ —5 mmol, and $Fe(NO_3)_3 \cdot 9H_2O$ —5 mmol). Citric acid monohydrate (40 mmol) was added slowly in the mixture with continuous stirring. Further, ethylene glycol (80 mmol) was added in the solution and stirred for 30 min. Afterward, the solution was stirred at the temperature of 180 °C to obtain gel followed by drying in an oven for 15 h at 140 °C. The sample was further decomposed in the furnace at different temperatures (650–1100 °C) to obtain Y_2NiFeO_6 .

The X-ray diffraction was performed with Rigaku MiniFlex X-ray diffractometer in the angle (2θ) range of 10°–80° using $Cu K_{\alpha 1}$ radiation ($\lambda = 1.54056 \text{ \AA}$) at the

scan speed of 2°/min. Particle size and morphology were observed by field emission electron microscopy (Hitachi HU-8010) at the operating voltage of 5 kV. Fourier transform infrared spectroscopy (FTIR) was performed by Bruker Alpha platinum-ATR to understand the chemical bonding. The presence of different oxidation states of elements in the material was analyzed by X-ray photoelectron spectroscopy (XPS) spectra recorded using instrument (XPS, Omicron Nano Technology, ESCA +). Magnetic properties were studied by analyzing M–H curves (at 5, 50, and 100 K) and M–T curves (field cooled (FC) at 2 kOe and zero field cooled (ZFC)) recorded using superconducting quantum interface device (SQUID) magnetometer (MPMS, XL, Quantum Design). Electrochemical experiments were performed in 6 M KOH aqueous solution with Ag/AgCl and platinum (Pt) as reference and counter electrodes, respectively, using potentiostat/galvanostat (Biologic SP-150). The slurry for making the working electrode was prepared by dissolving mixture of Y_2FeNiO_6 , acetylene black and polyvinylidene difluoride (PVDF) in the ratio of 8:1:1 in 20 ml of 1-methyl-2-pyrrolidinone with continuous stirring on a magnetic

stirrer for 15 h. Afterward, the working electrodes were prepared by uniform drop casting of the slurry on nickel mesh of area 1 cm^2 with mass loading of $\sim 1 \text{ mg}$ and subsequent evaporation afterward for 8 h in an oven at $80 \text{ }^\circ\text{C}$.

3 Results and discussion

3.1 Structural and morphological analysis

Figure 1a shows the X-ray diffraction (XRD) patterns of the double perovskite oxide Y_2NiFeO_6 synthesized at $650\text{--}1100 \text{ }^\circ\text{C}$. It is amorphous at the temperature of $650 \text{ }^\circ\text{C}$. As the temperature increases, it starts crystallizing, and at $850 \text{ }^\circ\text{C}$, both cubic and hexagonal phases with space group symmetries as $\text{Ia}3(206)$ and $\text{P}63/\text{mmc} (194)$ are formed [11,19]. With further increase of temperature to $950 \text{ }^\circ\text{C}$, the intensity of the peaks related to cubic phase increases. The hexagonal phase related peaks disappear and new peaks related to orthorhombic phase with $\text{Pnma} (62)$ space group symmetry emerge, indicating conversion

of hexagonal phase to orthorhombic phase at $950 \text{ }^\circ\text{C}$. With increase of temperature further to $1100 \text{ }^\circ\text{C}$, the intensity of peaks related to cubic phase increases further, but that of peaks related to orthorhombic phase decreases slightly, suggesting a further slow conversion of orthorhombic phase to cubic phase. Therefore, to retain the low temperature synthesis advantages such as less agglomeration of crystallites, smaller size and higher surface area, the thermally stable phase, synthesized at the temperature $950 \text{ }^\circ\text{C}$, was used for further investigation.

Figure 1b shows the XRD diffraction pattern of the sample synthesized at the temperature of $950 \text{ }^\circ\text{C}$. All the Bragg planes corresponding to different peaks have been indexed [10,11,19–25]. The average crystallite size estimated using Scherrer's formula (Eq. 1) was found to be $16 \pm 2 \text{ nm}$, $26 \pm 3 \text{ nm}$ and 32 ± 3 for the samples synthesized at $850 \text{ }^\circ\text{C}$, $950 \text{ }^\circ\text{C}$, $1100 \text{ }^\circ\text{C}$, respectively [25].

$$D = \frac{0.9\lambda}{\beta \cos\theta}, \quad (1)$$

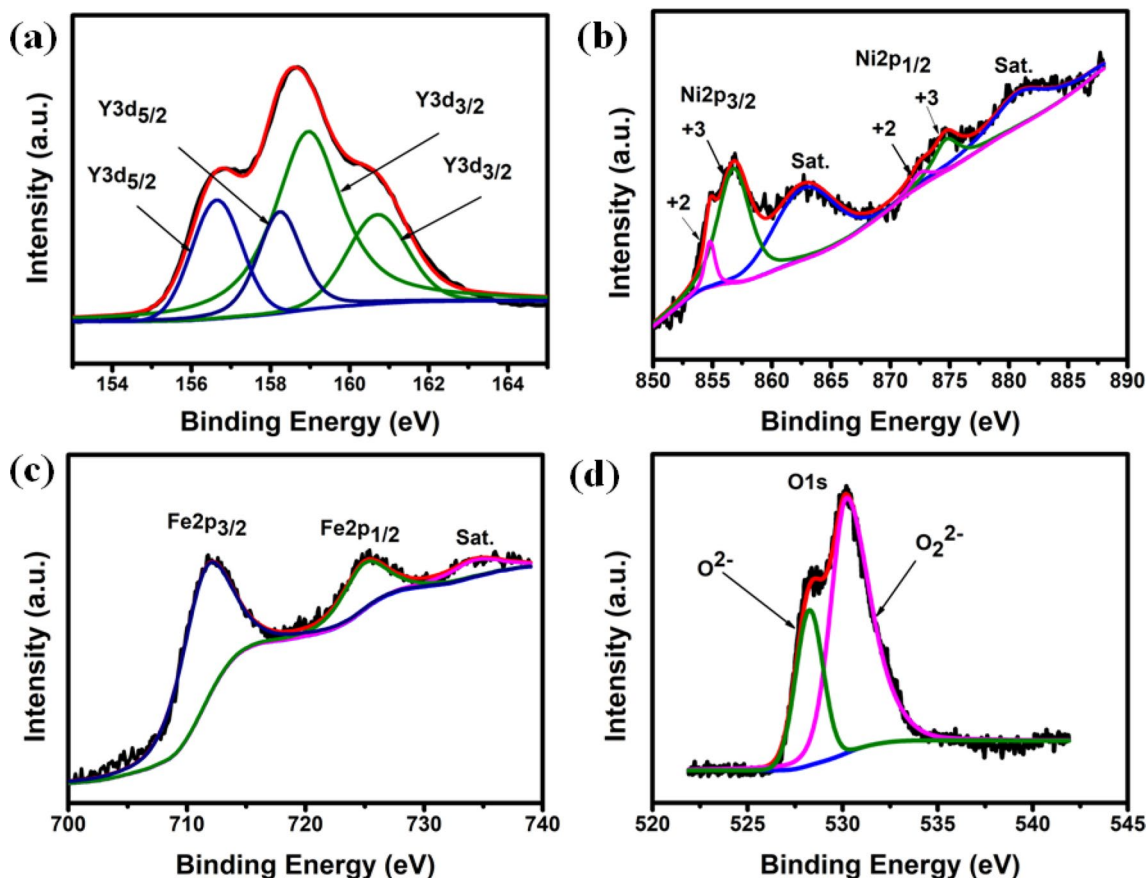


Fig. 2 X-ray photoelectron spectra of **a** $3d_{5/2}$ and $3d_{3/2}$ energy level of Y, **b** $2p_{3/2}$ and $2p_{1/2}$ energy level of Ni, **c** $2p_{3/2}$ and $2p_{1/2}$ energy level of Fe and **d** $1s$ energy level of oxygen in O in Y_2NiFeO_6

The tolerance factor (t) was calculated from the formula shown in Eq. 2 [14].

$$t = \frac{R_Y + R_O}{\sqrt{2} \left[\left(\frac{R_{Fe} + R_{Co}}{2} \right) + R_O \right]}, \quad (2)$$

where R_Y , R_{Ni} , R_{Fe} , and R_O represent the average ionic radii of elements Y, Ni, Fe and O, respectively. The estimated values for tolerance factor by considering the low and high spin states ionic radii for Ni^{3+} and Fe^{3+} are 0.869 and 0.9, respectively. The tolerance factor (t) between 0.7 and 0.9 corresponds to orthorhombic symmetry. If the value of t is 0.9 or close to 1, then structure becomes cubic. In our case, the calculated value of t supports the mixed orthorhombic and cubic symmetry, which is also confirmed from XRD patterns of high temperature stable phases.

Figure 1c shows the particle size distribution for Y_2NiFeO_6 powder sample, which is calculated from SEM image (inset of Fig. 1c). It reveals the formation of agglomerated grains of particle size between 75 and 325 nm. The average size calculated from SEM was 193 ± 7 nm. Figure 1d represents the Fourier transform infrared (FTIR) spectrum of Y_2NiFeO_6 . Its inset shows that there is no moisture or other impurities present in the sample. All the bands appearing between 400 and 600 cm^{-1} represent internal BO_6 modes present in the material. The broad peaks at 562 cm^{-1} and 527 cm^{-1} represent the Ni–O stretching vibration of $Ni-O_6$. The peak at 502 cm^{-1} corresponds to the stretching vibration of $Ni-O_6/FeO_6$. The modes between 436 and 490 cm^{-1} were ascribed to the oxygen octahedral bending vibrations of Fe–O in $Fe-O_6$ [11,26,27]. However, the band at 430 cm^{-1} represents the deformation vibration mode of Ni–O–Ni [28].

3.2 X-ray photoelectron spectroscopic analysis

X-ray photoelectron spectroscopy (XPS) has been used to study the oxidation states of different elements, Y, Fe, Ni and O, present on the surface of the Y_2NiFeO_6 . The XPS spectra have been fitted using XPSPEAK4.1 software by subtracting Shirley background. Figure 2a represents the XPS spectra for yttrium. Peaks appearing at 156.64 eV and 158.23 eV correspond to $Y3d_{5/2}$, and peaks appearing at 158.98 eV and 160.70 eV correspond to $Y3d_{3/2}$ confirming the presence of Y^{3+} [14,29]. Figure 2b represents the high-resolution spectra for nickel between the binding energy 850 eV and 890 eV. The peaks for $Ni2p_{3/2}$ appear at binding energies (854.79 eV, 856.80 eV) and for $Ni2p_{1/2}$ at binding energies (872.51 eV, 874.72 eV) with the corresponding satellite peaks at 862.70 eV and 880.90 eV, respectively, representing the presence of Ni^{2+}/Ni^{3+} states [11]. Figure 2c shows the peaks of $Fe2p_{3/2}$ at 711.50 eV, and $Fe2p_{1/2}$ at 724.90 eV with the satellite peak at 734.30 eV, representing the presence of iron in +3 oxidation state [14]. In Fig. 2d, the smaller peak at binding energy 528.25 eV corresponds to lattice oxygen (O^{2-}). The high intensity peak at 530.2 eV is assigned to reduced oxidation state of oxygen (O_2^{2-}) or to the oxygen vacancies present on the surface of Y_2NiFeO_6 [11,30].

3.3 Magnetic analysis

Figure 3a shows the variation of magnetic moment by cooling the sample from 300 to 5 K without the application of magnetic field (zero field cooled) and with application of magnetic field (field cooled) of 2 k Oe. Figure 3b shows

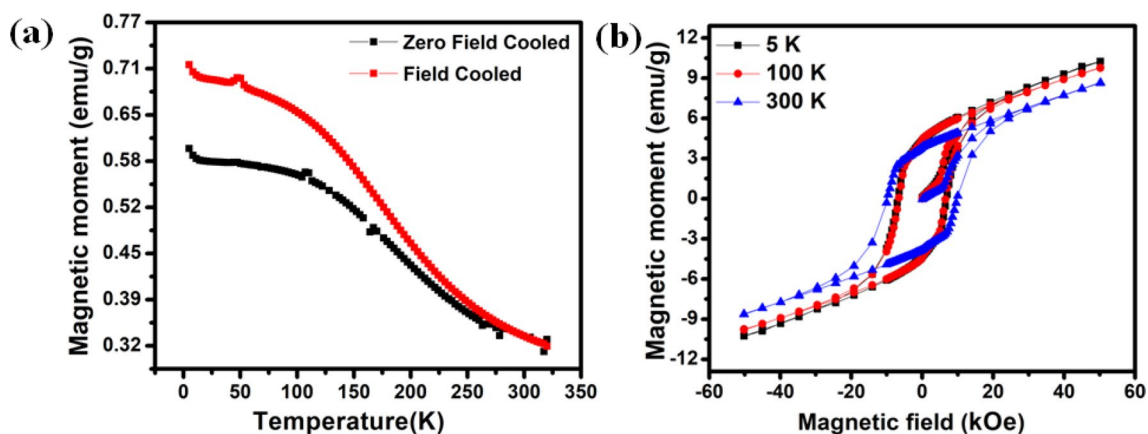


Fig. 3 a Variation of magnetic moment as a function of temperature with applied magnetic field of 2 kOe and b Variation of magnetic moment as a function of applied field at temperature of 5 K, 100 K and 300 K for Y_2NiFeO_6

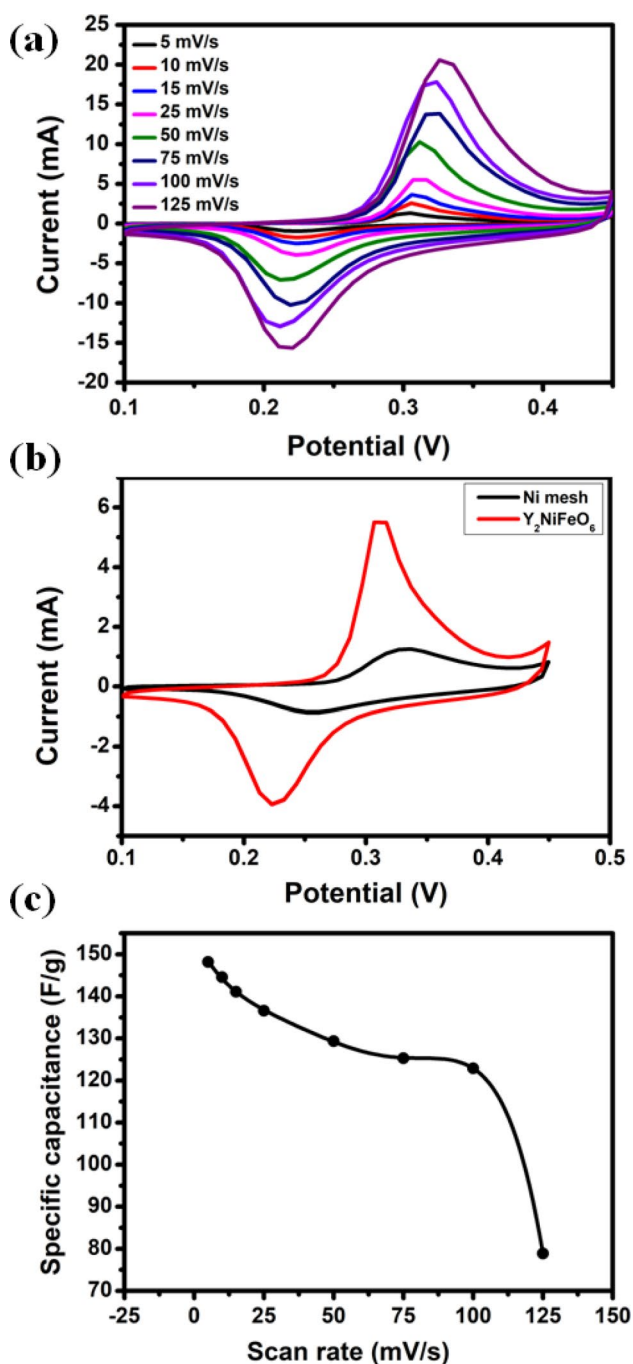


Fig. 4 **a** C–V curve for Y_2NiFeO_6 at different scan rates (5–125 mV/s), **b** C–V curve for Ni-Mesh and Y_2NiFeO_6 at scan rate of 25 mV/s, **c** variation of specific capacitance as a function of scan rate (calculated from CV curve)

the variation of magnetic moment with applied magnetic field (-50 to 50 kOe) at different temperatures of 5 K, 100 K, 300 K. The XPS study revealed the presence of Ni^{2+} ($t_{2g}^6e_g^2$)/ Ni^{3+} ($t_{2g}^5e_g^2$) and Fe^{3+} ($t_{2g}^3e_g^2$) on the surface of Y_2NiFeO_6 . The magnetism arises from the unpaired electrons in 3d levels of nickel and iron. There is no contribution

to magnetism from A site, because Y^{3+} has no unpaired electrons. It was previously reported that the material with magnetic anisotropy is dominated by intrinsic long-range ferromagnetic property. Therefore, the temperature at which zero field cooled (ZFC) and field cooled (FC) curves bifurcate gives the magnetic phase transition from paramagnetic to ferromagnetic temperature [31]. From Fig. 3a, it is clear that Curie temperature (T_c) is at or above 300 K. Further cusps with FWHM < 10 K observed at around 50 K and 110 K in ZFC and FC represents the spin blocking temperature and some changes associated with domain structure [32]. The FC magnetization is continuously increasing with cooling the sample, which shows that the material is highly anisotropic. Therefore, it is difficult to rotate the spins in the preferred direction by applying small magnetic field. Hence, the magnetic moment has low value as clear from Fig. 3a. The presence of high anisotropy further confirms the dominance of ferromagnetic behavior [33].

From hysteresis curves shown in Fig. 3b, it is clear that material is showing ferromagnetic behavior at and below room temperature. It confirms that it has Curie temperature at or above the room temperature. The isothermal saturation magnetization has been increasing from 8.66 to 10.25 emu/g with decrease of temperature from 300 to 5 K. The value of remanence increases from 3.84 to 4.36 emu/g and coercivity decrease from 9.84 to 6.92 kOe with decrease of temperature from 300 to 5 K (Fig. 3b). The isothermal saturation magnetization for Y_2NiFeO_6 is found to be larger than $YFeO_3$ [34]. The Curie temperature at or above room temperature makes the material a good candidate for nanomagnetic applications. The high value of saturation magnetization and high coercivity (9.84 kOe) at room temperature may be promising for magnetic data storage applications [35,36]. Further investigation of the properties such as magnetocaloric effect, magnetoresistance may reveal its potential towards application in magnetic refrigerants and spintronics [37,38].

3.4 Energy storage analysis

Energy storage analysis was performed using different techniques of cyclic voltammetry (CV), galvanostatic charge–discharge (GCD) and electrochemical impedance spectroscopy (EIS) in a conventional three-electrode system. Figure 4a represents the cyclic voltammetry (CV) curves performed in the potential range of (0.1 – 0.5 V) at different scan rates of (5 – 125 mV/s). The shape of the curves represents the pseudocapacitive behavior of Y_2NiFeO_6 representing the contribution from faradaic reactions. The oxidation and reduction reactions are due to presence of Ni and Fe. With the increase of scan rate, the cathodic and anodic peaks in CV shift toward more

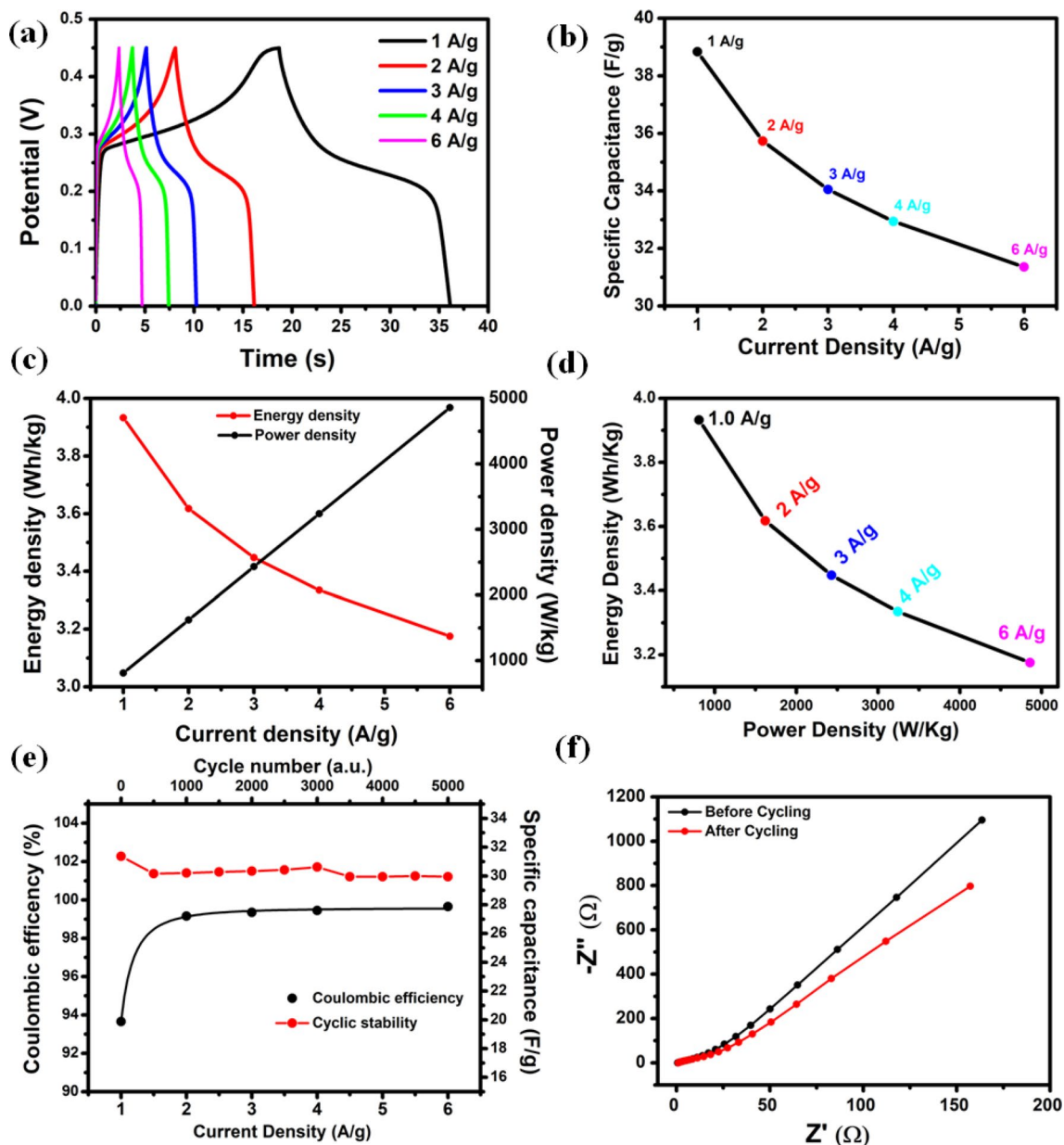


Fig. 5 **a** Galvanostatic charge–discharge curve at different current densities, **b** variation of specific capacitance (calculated from GCD) with current density, **c** variation of energy density and power density with current density, **d** variation of energy density with power den-

sity at different current densities (Ragone plot), **e** cyclic stability test for 5000 charging/discharging cycles, and coulombic efficiency and **f** electrochemical impedance spectrum (Nyquist plot) before and after cycling for Y_2NiFeO_6

positive and negative potential indicating fast redox reaction. It is important to note that increase of the scan rate does not alter the shape of CV curve. Such behavior of CV curve suggests the superior capacitive nature and enhanced rate capability [39].

The specific capacitance was calculated from CV curves using following equation [18]:

$$C_s = \frac{\int Idv}{2vm\Delta V}, \quad (3)$$

where ΔV represents the potential window, v the scan rate, m stands for the mass of active material (g), $\int Idv$ the area under the CV curve. The maximum value of the specific capacitance is 74.10 F/g at the scan rate of 5 mV/s. Figure 4b

Table 1 Comparison of Y_2NiFeO_6 electrochemical performance with other double perovskites

S. no	Electrode material	Method of synthesis	Specific capacitance (Fg^{-1})	Energy density (Whkg^{-1})	Power density (W kg^{-1})	Cyclic stability
1	Y_2NiFeO_6 [Present work]	Wet chemical sol-gel	74.10 at 5 mV/s	3.93 at 1A/g	810.03 at 1 A/g	95% at 6 A/g (5000 cycles)
2	Y_2CuMnO_6 [18]	Wet chemical sol-gel	79.4 at 5 mV/s	0.439 at 0.25 A/g	123.75 at 0.55 A/g	75% at 0.5 A/g (1000 cycles)
3	Y_2NiMnO_6 [17]	Wet chemical sol-gel	17.4 at 43.6 mA/g	0.197 at 10 mA/g	7.81 at 72.7 mA/g	85% at 43.6 mA/g (1800 cycles)
4	Y_2NiMnO_6 [17]	Hydrothermal	77.76 at 30 mA/g	0.89 at 30 mA/g	19.27 at 150 mA/g	70.17% at 30 mA/g (1800 cycles)
5	$\text{Sm}_2\text{NiMnO}_6$ [19]	Solvothermal	547.6 at 0.5 A/g	12.2 at 0.5 A/g	1000.7 at 6 A/g	86% at 4 A/g (1500 cycles)
6	$\text{La}_2\text{CuMnO}_6$ [20]	Hydrothermal	205.5 at 0.25 Ag^{-1}	–	–	78% at 1.5 A/g (1000 cycles)
7	$\text{La}_2\text{ZnMnO}_6$ [40]	Hydrothermal	515.5 at 0.5 Ag^{-1}	14.5 at 0.5 A/g	112.4 at 0.5 A/g	86% at 2.5 A/g (1000 cycles)

shows the CV curves for Ni mesh and Y_2FeNiO_6 at the scan rate of 25 mV/s for sake of comparison. It is clear from this figure that area under the curve for Ni mesh is very small as compared to Y_2NiFeO_6 electrodes and suggests a negligible contribution to capacitance. Figure 4c represents the variation of specific capacitance calculated from CV curves, as a function of scan rate. As the scan rate increases from 5 to 125 mV/s the specific capacitance decreases from 74.10 to 39.43 F/g. The decrease of specific capacitance is attributed to the unavailability of sufficient time for ions to get accommodated in active material. This reduces the storage of ions in active material and, in turn, a decrease of capacitance.

Figure 5(a) represents the galvanostatic charge–discharge (GCD) graph at different current densities of 1 A/g, 2 A/g, 3A/g, 4A/g and 6 A/g. It is clear from the figure that the discharging time is decreasing with the increase of current density. The important parameters to examine the energy storage performance of the material are specific capacitance, energy density, power density, and coulombic efficiency. All these parameters have been calculated from GCD via following equations [17,18]:

$$C_{sp} = \frac{I \times t_d}{m \times \Delta V}, \quad (4)$$

$$E_d = C_{sp} t_d^2 / 2, \quad (5)$$

$$P_d = \frac{3600 E_d}{t_d}, \quad (6)$$

$$\eta = \left(\frac{t_d}{t_c} \right) \times 100, \quad (7)$$

where I (mA) is current, ΔV (V) is the potential window and m (g) is mass of the active material of electrode and t_d , t_c (s) are the discharging and charging times. The specific capacitance calculated from Eq. 4 is 38.84 F/g, 35.73 F/g, 34.05 F/g, 32.94 F/g, and 31.36 F/g, respectively at the current density of 1 A/g, 2 A/g, 3 A/g, 4 A/g, and 6 A/g, respectively. Figure 5b represents the variation of specific capacitance calculated from GCD with current density. It shows that the specific capacitance decreases with increase of current density. Figure 5c represents the variation of energy density and power density with current density. As the current density increases from 1 to 6 A/g, the energy density decreases from 3.93 to 3.18 Wh/kg and the power density increases from 810.03 to 4860 W/kg. Figure 5d shows the Ragone plot exhibiting the variation of power density with energy density at different current densities. In Fig. 5e, black line represents the variation of Coulombic efficiency with current density and red line represents the cyclic stability for 5000 cycles at the current density of 6 A/g. Coulombic efficiency was found to increase from 93.66 to 99.65% with increase of current density from 1 to 6 A/g. It suggests the occurrence of diffusion controlled redox reactions. Specific capacitance retention has been found to be ~95% after 5000 charging- discharging cycles. The high value of specific capacitance retention makes this material a good candidate for energy storage application. In addition, the comparison of electrochemical performance of Y_2NiFeO_6 with other yttrium-based double perovskite (Table 1) shows that this material has better electrochemical performance than others in terms of energy density, power density, and cyclic stability. The lanthanide-based double perovskites such as $\text{Sm}_2\text{NiMnO}_6$, and $\text{La}_2\text{CuMnO}_6$, $\text{La}_2\text{ZnMnO}_6$ show better specific capacitance than yttrium-based double perovskites possibly due to high conductivity of lanthanides. The compound Y_2CoNiO_6 has been found to

have high specific capacitance value of 711 F/g at the current density of 1 A/g due to formation of conductive cubic phase [11]. Figure 5f represents the electrochemical impedance spectra (EIS) before and after 5000 cycles performed in the frequency range of 200 kHz–100 mHz with voltage amplitude of 10 mV. From z-fit of the data, the solution resistance (R_s) was found to increase from 0.66 to 0.993 Ω (after 5000 cycles) and the value of charge transfer resistance (R_{ct}) was found to increase from 11.6 to 19.5 Ω (after 5000 cycles).

4 Conclusions

Novel Y_2NiFeO_6 , synthesized via facile wet chemical route exhibited mixed phase structure from cubic hexagonal to cubic orthorhombic with increase of synthesis temperature. The mixed phase cubic-orthorhombic structure with space group symmetries $la\ 3$ (206) and $Pnma$ (62) was obtained at the temperature of 950 °C and above. As 950 °C was the lowest synthesis temperature to obtain thermally stable mixed phase of cubic-orthorhombic structure, the samples synthesized at this temperature were investigated for their structural, magnetic and energy storage properties. The XPS spectra showed the presence of yttrium in Y^{3+} state, nickel in Ni^{2+}/Ni^{3+} state and iron in Fe^{3+} state on the surface of the Y_2NiFeO_6 . The M–T and M–H curves confirmed ferromagnetic behavior with transition temperature T_c at or above the room temperature. The Y_2NiFeO_6 exhibited the highest specific capacitance 74.10 F/g at the scan rate of 5 mV/s from cyclic voltammetry and 38.84 F/g at the current density of 1 A/g from GCD in three-electrode system. The achieved values of energy and energy density at the current density of 1 A/g were ~ 3.93 Wh/kg and ~ 810.03 W/kg. Its coulombic efficiency has been found to increase from 93.66 to 99.65% with increase of current density from 1 A/g to 6 A/g. Specific capacitance retention has been found to be $\sim 95\%$ after 5000 charging–discharging cycles.

Acknowledgements The author (MD) thanks National Institute of Technology, Kurukshetra for providing Institute research fellowship. Author (AK²) acknowledges the support of CSIR New Delhi, India (F. No. 22(0778)/18/EMR-II).

References

1. S. Vasala, M. Karppinen, $A_2B'B''O_6$ perovskites: a review. *Prog. J. Solid State Chem.* **43**, 1–36 (2015). <https://doi.org/10.1016/j.progsolidstchem.2014.08.001>
2. J.E. Tasca, A.E. Lavat, M.G. González, Double perovskites La_2MMnO_6 as catalyst for propane combustion. *J. Asian Ceram. Soc.* **5**, 235–241 (2017). <https://doi.org/10.1016/j.jascer.2017.02.004>
3. N.S. Rogado, J. Li, A.W. Sleight, M.A. Subramanian, Magnetocapacitance and magnetoresistance near room temperature in a ferromagnetic semiconductor: La_2NiMnO_6 . *Adv. Mater.* **17**, 2225–2227 (2005). <https://doi.org/10.1002/adma.200500737>
4. K.-I. Kobayashi, T. Kimura, H. Sawada, K. Terakura, Y. Tokura, Room temperature magnetoresistance in an oxide material with an ordered double perovskite structure. *Nature* **395**, 677–680 (1998). <https://doi.org/10.1038/27167>
5. J. Zhang, W.J. Ji, J. Xu, X.Y. Geng, J. Zhou, Z.B. Gu, S.H. Yao, S.T. Zhang, Giant positive magnetoresistance in half-metallic double-perovskite Sr_2CrWO_6 thin films. *Sci. Adv.* **3**, e1701473 (2017). <https://doi.org/10.1126/sciadv.1701473>
6. J.A. Alonso, M.T. Casais, M.J. Martínez-Lope, J.L. Martínez, P. Velasco, A. Muñoz, M.T. Fernández-Díaz, Preparation, Crystal Structure, and magnetic and magnetotransport properties of the double perovskite Ca_2FeMoO_6 . *Chem. Mater.* **12**, 161–168 (2020). <https://doi.org/10.1021/cm990512g>
7. R. Pradheesh, H.S. Nair, V. Sankaranarayanan, K. Sethupathi, Large magnetoresistance and Jahn-Teller effect in Sr_2FeCoO_6 . *Phys. J. B Eur.* (2012). <https://doi.org/10.1140/epjb/e2012-30264-2>
8. Y. Jia, X. Zhang, Z. Zhang, L. Li, Effect of sintering temperature on microstructure and magnetic properties of double perovskite Y_2CoMnO_6 . *Ceram. Int.* **44**, 19794–19799 (2018). <https://doi.org/10.1016/j.ceramint.2018.07.236>
9. J. Su, Z.Z. Yang, X.M. Lu, J.T. Zhang, L. Gu, C.J. Lu, Q.C. Li, J.-M. Liu, J.S. Zhu, Magnetism-driven ferroelectricity in double perovskite Y_2NiMnO_6 . *ACS Appl. Mater. Inter.* **7**, 13260–13265 (2015). <https://doi.org/10.1021/acsami.5b00911>
10. G.R. Haripriya, S.P. Balmuchu, R. Pradheesh, The effect of particle size on the magnetic properties of Y_2FeCoO_6 . *Proc. Int. Conf. Nanotechnol. Better Living.* **3**, 173 (2016). <https://doi.org/10.3850/978-981-09-7519-7nbl16-rps-173>
11. M. Ickler, M. Devi, I. Rogge, J. Singh, A. Kumar, Ethylene glycol/citric acid stabilized wet chemically synthesized Y_2CoNiO_6 , and its structural, dielectric, magnetic and electrochemical behaviour. *Electron* **31**, 6977–6987 (2020). <https://doi.org/10.1007/s10854-020-03263-4>
12. H. Kozuka, K. Ohbayashi, K. Koumoto, Electronic conduction in La-based perovskite-type oxides. *Sci. Technol. Adv. Mater.* **16**, 026001 (2015). <https://doi.org/10.1088/1468-6996/16/2/026001>
13. Y.B. Wu, J. Bi, B.B. Wei, Preparation and supercapacitor properties of double-perovskite La_2CoNiO_6 inorganic nano-fibers. *Acta. Phys. - Chim. Sin.* **31**, 315 (2015). <https://doi.org/10.3866/PKU.WHXB201412164>
14. J. Singh, A. Kumar, Facile wet chemical synthesis and electrochemical behavior of La_2FeCoO_6 nano-crystallites. *Mater. Sci. Semicond. Process.* **99**, 8–13 (2019). <https://doi.org/10.1016/j.mssp.2019.04.007>
15. A. Kumar, A. Kumar, Electrochemical behavior of oxygen-deficient double perovskite, $Ba_2FeCoO_{6-\delta}$, synthesized by facile wet chemical process. *Ceram. Int.* **45**, 14105 (2019). <https://doi.org/10.1016/j.ceramint.2019.04.110>
16. Y. Liu, Z. Wang, J.P.M. Veder, Z. Xu, Y. Zhong, W. Zhou, M.O. Tade, S. Wang, Z. Shao, Highly defective layered double perovskite oxide for efficient energy storage via reversible pseudocapacitive oxygen-anion intercalation. *Adv. Energy Mater.* **8**, 1702604 (2018). <https://doi.org/10.1002/aenm.201702604>
17. M. Alam, K. Karmakar, M. Pal, K. Mandal, Electrochemical supercapacitor based on double perovskite Y_2NiMnO_6 nanowires. *RSC Adv.* **6**, 114722–114726 (2016). <https://doi.org/10.1039/C6RA23318J>
18. F.N. Mansoorie, J. Singh, A. Kumar, Wet chemical synthesis and electrochemical performance of novel double perovskite Y_2CuMnO_6 nanocrystallites. *Mater. Sci. Semicond. Process.* **107**, 104826 (2020). <https://doi.org/10.1016/j.mssp.2019.104826>

19. J. Singh, A. Kumar, Solvothermal synthesis dependent structural, morphological and electrochemical behaviour of mesoporous nanorods of Sm₂NiMnO₆. *Ceram. Int.* **46**, 11041–11048 (2020). <https://doi.org/10.1016/j.ceramint.2020.01.122>
20. J. Singh, U.K. Goutam, A. Kumar, Hydrothermal synthesis and electrochemical performance of nanostructured cobalt free La₂CuMnO₆. *Solid State Sci.* **95**, 105927 (2019). <https://doi.org/10.1016/j.solidstatedciences.2019.06.016>
21. W. Zhong, X.L. Wu, N.J. Tang, W. Liu, W. Chen, C.T. Au, Y.W. Du, Magnetocaloric effect in ordered double-perovskite Ba₂FeMoO₆ synthesized using wet chemistry. *Eur. Phys. J. B.* **217**, 213–217 (2004). <https://doi.org/10.1140/epjb/e2004-00312>
22. F. Liu, J. Li, Q. Li, Y. Wang, X. Zhao, Y. Hua, C. Wang, X. Liu, High pressure synthesis, structure, and multiferroic properties of two perovskite compounds Y₂FeMnO₆ and Y₂CrMnO₆. *Dalton T.* **43**, 1691–1698 (2014). <https://doi.org/10.1039/c3dt52336e>
23. R. Mohassel, A. Sobhani, M. Salavati-Niasari, M. Goudarzi, Pechini synthesis and characteristics of Gd₂CoMnO₆ nanostructures and its structural, optical and photocatalytic properties. *Spectrochim. Acta A.* **204**, 232–240 (2018). <https://doi.org/10.1016/j.saa.2018.06.050>
24. M. Ismael, E. Elhaddad, D.H. Taffa, M. Wark, Synthesis of phase pure hexagonal YFeO₃ perovskite as efficient visible light active photocatalyst. *Catalysts* **7**, 326 (2017). <https://doi.org/10.3390/catal7110326>
25. F.S. Al-Hazmi, A.A. Al-Ghamdi, L.M. Bronstein, L.S. Memesh, F.S. Shokr, M. Hafez, The influence of sintering temperature on the structure, optical and magnetic properties of yttrium iron oxide YFeO₃ prepared via α-alanine assisted combustion method. *Ceram. Int.* **43**, 8133–8138 (2017). <https://doi.org/10.1016/j.ceramint.2017.03.137>
26. A.A. Kumar, A. Kumar, J.K. Quamara, Cetyltrimmonium bromide assisted synthesis of lanthanum containing barium stannate nanoparticles for application in dye sensitized solar cells. *Phys. Status Solidi A.* **215**, 1700723 (2018). <https://doi.org/10.1002/pssa.201700723>
27. C. Jagadeeshwaran, A.P.B. Selvadurai, V. Pazhanivelu, R. Murugaraj, Structure, optical and magnetic behavior of LaFeO₃ and LaFe_{0.9}Ni_{0.1}O₃ by combustion method. *Int. J. Innov. Res. Sci. Eng.* (2013). <https://doi.org/10.13140/2.1.1506.4966>
28. M. Sivakumar, K. Pandi, S.M. Chen, Y.H. Cheng, M. Sakthivel, Facile synthesis of perovskite-type NdNiO₃ nanoparticles for effective electrochemical non-enzymatic glucose biosensor. *New J. Chem.* **41**, 11201–11207 (2017). <https://doi.org/10.1039/x0xx00000x>
29. K. Datta, R.B. Neder, J. Chen, J.C. Neuefeind, B. Mihailova, Atomic-level structural correlations across the morphotropic phase boundary of a ferroelectric solid solution: xBiMg_{1/2}Ti_{1/2}O₃-(1-x)PbTiO₃. *Sci. Rep.* **7**, 471 (2017). <https://doi.org/10.1038/s41598-017-00530-z>
30. N. Basavegowda, K. Mishra, R.S. Thombal, K. Kaliraj, Y.R. Lee, Sonochemical green synthesis of yttrium oxide (Y₂O₃) nanoparticles as a novel heterogeneous catalyst for the construction of biologically interesting 1,3-Thiazolidin – 4-ones. *Catal. Lett.* **147**, 2630–2639 (2017). <https://doi.org/10.1007/s10562-017-2168-4>
31. H. Xia, D. Zhu, Z. Luo, Y. Yu, X. Shi, G. Yuan, J. Xie, Hierarchically structured Co₃O₄@Pt@MnO₂ nanowire arrays for high-performance supercapacitors. *Sci. Rep.* **3**, 1–8 (2013). <https://doi.org/10.1038/srep02978>
32. P.A. Joy, P.S.A. Kumar, S.K. Date, The relationship between field-cooled and zero-field-cooled susceptibilities of some ordered magnetic systems. *J. Phys. Condens. Matter* **10**, 11049–11054 (1998). <https://doi.org/10.1088/0953-8984/10/48/024>
33. F. Huang, Z. Wang, X. Lu, J. Zhang, K. Min, W. Lin, R. Ti, T.T. Xu, J. He, C. Yue, J. Zhu, Peculiar magnetism of BiFeO₃ nanoparticles with size approaching the period of the spiral spin structure. *Sci. Rep.* **3**, 2907 (2017). <https://doi.org/10.1038/srep02907>
34. H. Shen, J. Xu, A. Wu, J. Zhao, M. Shi, Magnetic and thermal properties of perovskite YFeO₃ single crystals. *Adv. Mat. Sci. Eng. B.* **157**, 77–80 (2009). <https://doi.org/10.1016/j.mseb.2008.12.020>
35. S. Hirosawa, M. Nishino, S. Miyashita, Perspectives for high-performance permanent magnets: applications, coercivity, and new materials. *Adv. Nat. Sci. - Nanosci.* **8**, 13002 (2017). <https://doi.org/10.1088/2043-6254/aa597c>
36. C. Tannous, R.L. Comstock, Magnetic information-storage materials, in *Springer handbook of electronic and photonic materials*. *Springer handbooks*, ed. by S. Kasap, P. Capper (Springer, Cham, 2017), pp. 1–1. https://doi.org/10.1007/978-3-319-48933-9_49
37. V. Chaudhary, R.V. Ramanujan, Magnetocaloric properties of Fe-Ni-Cr nanoparticles for active cooling. *Sci. Rep.* **6**, 35156 (2016). <https://doi.org/10.1038/srep35156>
38. S. Tehrani, E. Chen, M. Durlam, M. DeHerrera, J.M. Slaughter, J. Shi, G. Kerszykowski, High density submicron magnetoresistive random access memory (invited). *J. Phys.* **85**, 5822 (1999). <https://doi.org/10.1063/1.369931>
39. J. Zhang, Y. Sun, X. Li, J. Xu, Fabrication of porous NiMn₂O₄ nanosheet arrays on nickel foam as an advanced sensor material for non-enzymatic glucose detection. *Sci. Rep.* **9**, 18121 (2019). <https://doi.org/10.1038/s41598-019-54746-2>
40. J. Singh, A. Kumar, U.K. Goutam, A. Kumar, Microstructure and electrochemical performance of La₂ZnMnO₆ nanoflakes synthesized by facile hydrothermal route. *Appl. Phys. A.* **126**, 11 (2020). <https://doi.org/10.1007/s00339-019-3195-3>

Publisher's Note Springer Nature remains neutral with regard to jurisdictional claims in published maps and institutional affiliations.